

End2End Multi-View Feature Matching using Differentiable Pose Optimization

Barbara Roessle and Matthias Nießner

Technical University of Munich

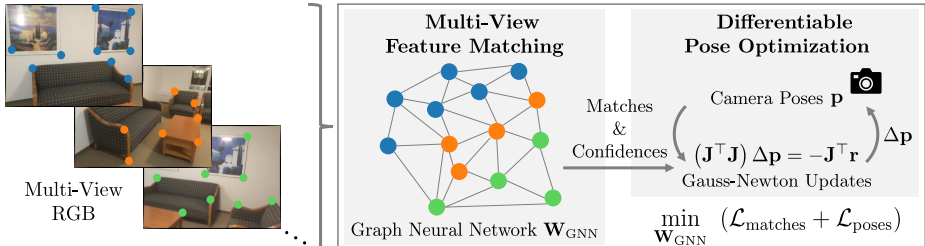


Fig. 1. We connect feature matching and pose optimization in an end-to-end trainable pipeline that enables matches and confidence weights to be informed by the pose estimation objective. To this end, we introduce GNN-based multi-view feature matching to inform pose optimization with a differentiable pose solver, which increases both pose estimation and matching accuracy.

Abstract. Learning-based approaches have become indispensable for camera pose estimation. However, feature detection, description, matching, and pose optimization are often approached in an isolated fashion. In particular, erroneous feature matches have severe impact on subsequent camera pose estimation and often require additional measures such as outlier rejection. Our method tackles this challenge by addressing feature matching and pose optimization jointly: first, we integrate information from multiple views into the matching by spanning a graph attention network across multiple frames to predict their matches all at once. Second, the resulting matches along with their predicted confidences are used for robust pose optimization with a differentiable Gauss-Newton solver. End-to-end training combined with multi-view feature matching boosts the pose estimation metrics compared to SuperGlue by 8.9% on ScanNet and 10.7% on MegaDepth on average. Our approach improves both pose estimation and matching accuracy over state-of-the-art matching networks. Training feature matching across multiple views with gradients from pose optimization naturally learns to disregard outliers, thereby rendering additional outlier handling unnecessary, which is highly desirable for pose estimation systems.

1 Introduction

Feature matching is a key component in many 3D vision applications such as structure from motion (SfM) or simultaneous localization and mapping (SLAM).

Conventional pose estimation is a multi-step process: feature detection finds interest points, for which local descriptors are computed. Based on the descriptors, pairs of keypoints from different images are matched, which defines constraints in the pose optimization. A major challenge lies in the ambiguity of matching local descriptors by nearest-neighbor search, which is error-prone, particularly in texture-less areas or in presence of repetitive patterns. Hand-crafted heuristics or outlier filters become necessary to circumvent this problem to some degree.

Recent learning-based approaches [36,38,21] instead leverage the greater image context to address the matching difficulty, e.g., SuperGlue [36] introduces a graph neural network (GNN) for descriptor matching on an image pair. Graph edges connect keypoints from arbitrary locations and enable reasoning in a broad context, leading to globally well informed solutions compared to convolutional neural networks (CNN) with limited receptive field. The receptive field in SuperGlue, however, remains limited by the two-view setup, despite that more images are typically available in pose estimation tasks. Our idea is to further facilitate information flow by joining multiple views into the matching process. This way, we allow multi-view correlation to strengthen geometric reasoning and confidence prediction. Joint matching of multiple images integrates well into pose estimation pipelines, as they typically solve for more than two cameras.

Additionally, we note that accurate feature matching, in and of itself, does not necessarily give rise to accurate pose estimation, as the spatial distribution of feature matches is essential for robust pose optimization. For instance, perfectly precise matches may form a degenerate case (e.g., lying on a line) and thus have no value for pose optimization. In addition, confidence scores predicted by matching networks do not necessarily reflect the value of matches towards pose optimization. Feature matching and pose estimation are thus tightly coupled problems, for which we propose a joint solution:

We encode keypoints and descriptors from multiple images to construct a graph, where self-attention provides context awareness within the same image and cross-attention enables reasoning with respect to all other images. A GNN predicts matches along with confidence weights, which define constraints on the camera poses that we optimize with a differentiable Gauss-Newton solver. The GNN is trained end-to-end using gradients from the pose optimization. From this feedback, the network learns to produce valuable matches for pose estimation and thereby learns effective outlier rejection. We evaluate our method on the ScanNet [12], Matterport3D [9] and MegaDepth [24] datasets and show that it improves over prior work on learned feature matching.

In summary, we demonstrate that a joint approach to feature matching and pose estimation benefits both matching and pose accuracy, enabled by the following contributions:

- We propose a multi-view graph attention network to learn feature matches simultaneously across multiple frames.
- We introduce an end-to-end trainable pose estimation that both guides confidence weights of feature matches in an unsupervised fashion and backpropagates gradients to inform the graph-matching network.

2 Related Work

Conventional Feature Matching. The classical feature matching pipeline comprises the following steps: 1) interest point detection, 2) feature description, 3) matching through nearest neighbor search in descriptor space, and 4) outlier filtering. In this pipeline, hand-crafted features like SIFT [26] and ORB [35] are very successful and have been widely used for many years. However, they tend to struggle with appearance or viewpoint changes. Starting with LIFT [45], learning-based descriptors have been developed to tackle these challenges [28,15,32,3,42]. They often combine interest point detection and description, such as SuperPoint [14], which we use for our method. Nearest neighbor feature matching is prone to outliers, making post-processing methods indispensable. This includes mutual check, ratio test [26], neighborhood consensus [41,8,7,4,27] and sampling based outlier rejection [17,2,30]. Learning-based approaches have also addressed outlier detection as a classification task [46,31,6,48]. These methods rely on reasonable matching proposals and lack visual information in their decision process.

Learning-based Feature Matching. Recent approaches employ neural networks for feature matching on image pairs. There are methods that determine dense, pixel-wise correspondences with confidence estimates for filtering [34,33,23]. This effectively combines steps (1)-(3) from the classical matching pipeline. However, it suffers from the limited receptive field of CNNs and fails to distinguish regions of little texture or repetitive structure, due to missing global context. In contrast, SuperGlue [36] represents a sparse matching network that operates on keypoints with descriptors. Using an attention-based GNN [44] all keypoints interact, hence the receptive field spans across both images, leading to accurate matches in wide-baseline settings. Inspired by the success of GNN-based feature matching, we build up on SuperGlue by further extending its receptive field through multi-view matching and by improving outlier filtering through end-to-end training with pose optimization. LoFTR [38] recently proposed a detector-free approach, that processes CNN features in a coarse-to-fine manner. Combined with attention it equally achieves a receptive field across the image pair and high quality matches. COTR [21], like LoFTR, operates on images directly in a coarse-to-fine fashion. It is a transformer network that predicts for a query point in one image the correspondence in a second image. This way, it considers the global context; however, inference for a complete image pair takes tens of seconds. We show that our multi-view, end-to-end approach performs better than SuperGlue and the detector-free methods LoFTR and COTR.

Pose Optimization. Once matches between a set of images are found, poses can be optimized using a bundle adjustment formulation [40]. The optimization can be applied to a set of RGB images [1] or lifted to the RGB-D case, if depth data is available from range sensors [13]. The resulting optimization problems typically lead to non-linear least squares formulations which are optimized using

non-linear solvers such as Gauss-Newton or Levenberg-Marquardt. The pipeline in these methods usually performs feature matching as a pre-process; i.e., correspondences are established first and then filtered with a combination of RANSAC and robust optimization techniques [47,10]. However, feature matching and pose optimization largely remain separate steps and cannot inform each other.

To this end, differentiable optimization techniques have been proposed for pose estimation, such as DeMoN [43], BA-Net [39], RegNet [20], or 3DRegNet [29]. The core idea of these methods is to obtain gradients through the pose optimizations that in turn guide the construction of learned feature descriptors. In comparison to treating feature extraction as a separate step, feature descriptors are now learned with the objective to obtain well-aligned global poses instead of just trying to get good pair-wise matches. In our work, we go a step further and focus on learning how to match features rather than using a pre-defined matching method.

As a result, we can leverage differentiable pose optimization to provide gradients for our newly-proposed multi-view graph attention network for feature matching, and achieve significantly improved pose estimation results.

3 Method

Our method associates keypoints from N images $\{I_n\}_{n=1}^N$, such that resulting matches and confidence weights are particularly valuable for estimating the corresponding camera poses $\{\mathbf{p}_n\}_{n=1}^N$, $\mathbf{p}_n \in \mathbb{R}^6$. Keypoints are represented by their image coordinates $\mathbf{x} \in \mathbb{R}^2$, visual descriptors $\mathbf{d} \in \mathbb{R}^D$ and a confidence score $c \in [0, 1]$. We use the SuperPoint network for feature detection and description, as it has shown to perform well in combination with learned feature matching [14,36]. The source of input descriptors, however, is flexible; for instance, the use of conventional descriptors, such as SIFT [26], is also possible.

Our pipeline, as shown in Fig. 1, ties together feature matching and pose optimization: we employ a GNN to associate keypoints across multiple images (Sec. 3.1). The resulting matches and confidence weights define constraints in the subsequent pose optimization (Sec. 3.2), which is differentiable, thus enabling end-to-end training (Sec. 3.3).

3.1 Graph Attention Network for Multi-View Matching

Motivation. In the multi-view matching problem of N images, each keypoint matches to at most $N - 1$ other keypoints, where each of the matching keypoints has to come from a different input image. Without knowing the transformations between images, one keypoint can match to any keypoint location in the other images. Hence, all keypoints in the other images need to be considered as matching candidates. Although keypoints from the same image are not matching candidates, they contribute valuable constraints in the assignment problem, e.g., their projection into other images must follow consistent transformations. The matching problem can be represented as a graph, where nodes

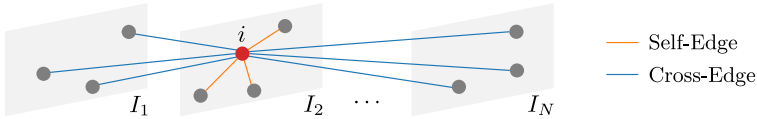


Fig. 2. Self- and cross-edges connected to a node i .

model keypoints and edges their relationships. A GNN architecture reflects this structure and enables learning the complex relations between keypoints to determine feature matches. The iterative message passing process enables the search for globally optimal matches as opposed to a greedy local assignment. On top of that, attention-based message aggregation allows each keypoint to focus on information from the keypoints that provide the most insight for its assignment. We build upon the SuperGlue architecture, which introduces an attention-based GNN for descriptor matching between image pairs [36]. Our extension to multi-image matching is motivated by the following considerations: first, graph-based reasoning can benefit from tracks that are longer than two keypoints—i.e., a match becomes more confident, if multiple views agree on the keypoint similarity and its coherent location with respect to the other keypoints in each frame. In particular, with regards to robust pose optimization, it is crucial to facilitate this information flow and boost the confidence prediction. Second, pose estimation or SLAM systems generally consider multiple input views. With the described graph structure, jointly matching N images is more efficient in terms of GNN messages than matching the corresponding image pairs individually, as detailed in the following paragraph.

Graph Construction. Each keypoint represents a graph node. The initial node embedding ${}^{(1)}\mathbf{f}_i$ of keypoint i is computed from its image coordinates \mathbf{x}_i , confidence c_i and descriptor \mathbf{d}_i (Eq. (1)). This allows the GNN to consider spatial location, certainty and visual appearance in the matching process:

$${}^{(1)}\mathbf{f}_i = \mathbf{d}_i + F_{\text{encode}}([\mathbf{x}_i \parallel c_i]), \quad (1)$$

where \parallel denotes concatenation and F_{encode} is a multilayer perceptron (MLP) that lifts the image point and its confidence into the high-dimensional space of the descriptor. Such positional encoding helps the spatial learning [36, 18, 44]. The graph nodes are connected by two kinds of edges: self-edges connect keypoints within the same image. Cross-edges connect keypoints from different images (Fig. 2). The edges are undirected, i.e., information flows in both directions. Tab. 1 shows that jointly matching N images reduces the number of GNN messages compared to separately matching the corresponding $P = \sum_{n=1}^{N-1} n$ pairs. The savings result from fewer intra-frame messages between keypoints of the same image, e.g., for five images with K keypoints each, pairwise matching involves $20K^2$ messages on a self-layer and $20K^2$ on a cross-layer—joint matching requires only $5K^2$ and $20K^2$, respectively.

Table 1. Number of GNN messages per layer for matching N images, each with K keypoints, as P individual image pairs versus joint matching in a single graph.

	Messages along self-edges	Messages along cross-edges
Pairwise matching	$2PK^2$	$N(N-1)K^2$
Joint matching	NK^2	$N(N-1)K^2$

Message Passing. Interaction between keypoints—the graph nodes—is realized through message passing [16,19]. The goal is to achieve a state where node descriptors of matching keypoints are close in descriptor space, whereas unrelated keypoints are far apart. The GNN has L layers, where each layer ℓ corresponds to a message exchange between keypoints. The layers alternate between updates along self-edges $\mathcal{E}_{\text{self}}$ and cross-edges $\mathcal{E}_{\text{cross}}$ —starting with an exchange along self-edges in layer $\ell = 1$ [36]. Eq. (2) describes the iterative node descriptor update, where $^{(\ell)}\mathbf{m}_{\mathcal{E} \rightarrow i}$ is the aggregated message from all keypoints that are connected to keypoint i by an edge in $\mathcal{E} \in \{\mathcal{E}_{\text{self}}, \mathcal{E}_{\text{cross}}\}$. $^{(\ell)}F_{\text{update}}$ is a MLP, where each GNN layer ℓ has a separate set of network weights.

$$^{(\ell+1)}\mathbf{f}_i = ^{(\ell)}\mathbf{f}_i + ^{(\ell)}F_{\text{update}} \left(\left[^{(\ell)}\mathbf{f}_i \parallel ^{(\ell)}\mathbf{m}_{\mathcal{E} \rightarrow i} \right] \right) \quad (2)$$

Multi-head attention [44] is used to merge all incoming information for keypoint i into a single message $^{(\ell)}\mathbf{m}_{\mathcal{E} \rightarrow i}$ [36]. Messages along self-edges are combined by self-attention between the keypoints of the same image, messages along cross-edges by cross-attention between the keypoints from all other images. Linear projection of node descriptors is used to compute the query $^{(\ell)}\mathbf{q}_i$ of query keypoint i , as well as the keys $^{(\ell)}\mathbf{k}_j$ and values $^{(\ell)}\mathbf{v}_j$ of its source keypoints j :

$$^{(\ell)}\mathbf{q}_i = ^{(\ell)}\mathbf{W}_1 ^{(\ell)}\mathbf{f}_i + ^{(\ell)}\mathbf{b}_1, \quad (3)$$

$$\begin{bmatrix} ^{(\ell)}\mathbf{k}_j \\ ^{(\ell)}\mathbf{v}_j \end{bmatrix} = \begin{bmatrix} ^{(\ell)}\mathbf{W}_2 \\ ^{(\ell)}\mathbf{W}_3 \end{bmatrix} ^{(\ell)}\mathbf{f}_j + \begin{bmatrix} ^{(\ell)}\mathbf{b}_2 \\ ^{(\ell)}\mathbf{b}_3 \end{bmatrix}. \quad (4)$$

The set of source keypoints $\{j : (i, j) \in \mathcal{E}\}$ comprises all keypoints connected to i by an edge of the type, that is relevant to the current layer. \mathbf{W} and \mathbf{b} are per-layer weight matrices and bias vectors, respectively. For each source keypoint the similarity to the query is computed by the dot product $^{(\ell)}\mathbf{q}_i \cdot ^{(\ell)}\mathbf{k}_j$. The softmax over the similarity scores determines the attention weight α_{ij} of each source keypoint j in the aggregated message to i :

$$^{(\ell)}\mathbf{m}_{\mathcal{E} \rightarrow i} = \sum_{j:(i,j) \in \mathcal{E}} ^{(\ell)}\alpha_{ij} ^{(\ell)}\mathbf{v}_j. \quad (5)$$

It is important to note that in layers, which update along cross-edges, the source keypoints j to a query keypoint i come from multiple images. The softmax-based weighting is robust to variable number of input views and therewith variable number of keypoints. After L message passing iterations the node descriptors for subsequent assignment are retrieved by linear projection:

$$\mathbf{f}_i = \mathbf{W}_4 ^{(L+1)}\mathbf{f}_i + \mathbf{b}_4. \quad (6)$$

Partial Assignment. SuperGlue [36] addresses the partial assignment problem between keypoints of two images, I_1 and I_2 , where each keypoint either obtains a match in the other image or remains unmatched. A score matrix $\mathbf{S} \in \mathbb{R}^{(K_1+1) \times (K_2+1)}$ is defined, where K_1 and K_2 are the number of keypoints in the images, hence all potential matches and the unmatched option are represented. The elements $\mathbf{S}_{i,j}$ are filled with the dot-product similarity of the final node descriptors $\mathbf{f}_{1,i} \cdot \mathbf{f}_{2,j}$, where $\mathbf{f}_{1,i}$ is from I_1 and $\mathbf{f}_{2,j}$ from I_2 . The last row and column of \mathbf{S} , representing unmatched, are initialized with a trainable parameter $q \in \mathbb{R}$. The differentiable Sinkhorn algorithm [37,11] optimizes for a soft assignment matrix $\mathbf{P} \in [0, 1]^{(K_1+1) \times (K_2+1)}$ that maximizes the sum of scores $\sum_{r,c} \mathbf{S}_{r,c} \mathbf{P}_{r,c}$ while obeying constraints on the number of matches:

$$\mathbf{P} \mathbf{1}_{K_2+1} = [\mathbf{1}_{K_1+1}^\top K_2]^\top \quad \text{and} \quad \mathbf{P}^\top \mathbf{1}_{K_1+1} = [\mathbf{1}_{K_2+1}^\top K_1]^\top. \quad (7)$$

We adopt this approach and apply it pairwise to the images in the multi-view setting. \mathcal{P} is the set of all possible image pairs from $\{I_n\}_{n=1}^N$, excluding pairs between identical images, as well as pairs that are a permutation of an existing pair. For each pair $(a, b) \in \mathcal{P}$, where $a, b \in \{1, 2, \dots, N\}$, a score matrix \mathbf{S}_{ab} is created and the assignment \mathbf{P}_{ab} is computed by means of Sinkhorn algorithm. From \mathbf{P}_{ab} the set of matches \mathcal{M}_{ab} is derived: first, a candidate match for each keypoint in I_a and I_b is determined by the row-wise and column-wise maximal elements of \mathbf{P}_{ab} . Second, mutual agreement of matching keypoints is enforced.

3.2 Differentiable Pose Optimization

We introduce a differentiable optimizer Ω that jointly estimates all camera poses from the matches determined by the partial assignment:

$$\{\mathbf{p}_n\}_{n=1}^N = \Omega(\{\mathcal{M}_{ab} : (a, b) \in \mathcal{P}\}, \{Z_n\}_{n=1}^N). \quad (8)$$

To stabilize the optimization, we use the depth maps $\{Z_n\}_{n=1}^N$ as additional input. Without depth measurements or good pose initialization, the optimization of bundle adjustment formulations is prone to fall into local minima.

We define the energy as weighted sum of squared errors between matches in world coordinates (Eq. (9)). A match consists of the image coordinates, \mathbf{x}_a in I_a and \mathbf{x}_b in I_b , as well as the matching confidence w , i.e., the corresponding element from the assignment \mathbf{P}_{ab} . The function $\pi_n^{-1}(\mathbf{x}_n, Z_n)$ unprojects an image point \mathbf{x}_n in I_n to homogeneous camera coordinates using its depth from Z_n . $\mathbf{T}_{\mathbf{p}_n} \in \mathbb{R}^{3 \times 4}$ defines the transformation from camera pose \mathbf{p}_n to world coordinates. $\mathbf{p} \in \mathbb{R}^{6N}$ refers to the concatenation of all pose vectors, which are in $\mathfrak{se}(3)$ coordinates, i.e., three translation elements followed by three rotation elements.

$$E(\mathbf{p}) = \sum_{(a,b) \in \mathcal{P}} \sum_{(\mathbf{x}_a, \mathbf{x}_b, w) \in \mathcal{M}_{ab}} w^2 \|\mathbf{T}_{\mathbf{p}_a} \mathbf{y}_a - \mathbf{T}_{\mathbf{p}_b} \mathbf{y}_b\|_2^2, \quad (9)$$

$$\text{where } \mathbf{y}_a = \pi_a^{-1}(\mathbf{x}_a, Z_a) \quad \text{and} \quad \mathbf{y}_b = \pi_b^{-1}(\mathbf{x}_b, Z_b). \quad (10)$$

Gauss-Newton is used to minimize the energy with respect to the camera poses. For this purpose, a residual vector $\mathbf{r} \in \mathbb{R}^{3M}$ is created from the energy terms, where M is the total number of matches between all images. Each match m fills its corresponding subvector $\mathbf{r}_m \in \mathbb{R}^3$:

$$\mathbf{r}_m = w(\mathbf{T}_{\mathbf{p}_a} \mathbf{y}_a - \mathbf{T}_{\mathbf{p}_b} \mathbf{y}_b). \quad (11)$$

All poses are initialized to $\mathbf{0}$. We keep one pose fixed, which defines the world frame, and optimize for the remaining poses $\bar{\mathbf{p}} \in \mathbb{R}^{6(N-1)}$. The Jacobian matrix $\mathbf{J} \in \mathbb{R}^{3M \times 6(N-1)}$ is initialized to $\mathbf{0}$ and filled with the partial derivatives with respect to the pose parameters: for each match m the corresponding blocks $\mathbf{J}_{ma}, \mathbf{J}_{mb} \in \mathbb{R}^{3 \times 6}$ are assigned [5]:

$$\mathbf{J}_{ma} = \frac{\partial \mathbf{r}_m}{\partial \mathbf{p}_a} = w [\mathbf{I}_3 \quad -(\mathbf{T}_{\mathbf{p}_a} \mathbf{y}_a)^\wedge] \quad , \quad \mathbf{J}_{mb} = \frac{\partial \mathbf{r}_m}{\partial \mathbf{p}_b} = w [-\mathbf{I}_3 \quad (\mathbf{T}_{\mathbf{p}_b} \mathbf{y}_b)^\wedge]. \quad (12)$$

\mathbf{I}_3 is a 3×3 identity matrix and $(\cdot)^\wedge$ maps a vector $\in \mathbb{R}^3$ to its skew-symmetric matrix: $\begin{bmatrix} x \\ y \\ z \end{bmatrix} \rightarrow \begin{bmatrix} 0 & -z & y \\ z & 0 & -x \\ -y & x & 0 \end{bmatrix}$. If a or b identify the fixed pose, the corresponding assignment to \mathbf{J} is skipped. Using the current state of the camera poses, each Gauss-Newton iteration establishes a linear system, that is solved for the pose update $\Delta \bar{\mathbf{p}}$ using LU decomposition:

$$\mathbf{J}^\top \mathbf{J} \Delta \bar{\mathbf{p}} = -\mathbf{J}^\top \mathbf{r}. \quad (13)$$

We update the poses in $T = 10$ Gauss-Newton iterations, from which the set of poses with minimal energy is used for end-to-end training in Sec. 3.3.

3.3 End-to-End Training

The learnable parameters include the GNN parameters and the parameter q of the partial assignment module. The whole pipeline, from the matching network to the pose optimization, is differentiable, which allows for a pose loss that guides the matching network to produce valuable matches and accurate confidences for robust pose optimization. The training objective \mathcal{L} consists of a matching term $\mathcal{L}_{\text{match}}$ [36] and a pose term $\mathcal{L}_{\text{pose}}$, which are balanced by the factor λ :

$$\mathcal{L} = \sum_{(a,b) \in \mathcal{P}} \mathcal{L}_{\text{match}}(a,b) + \lambda \mathcal{L}_{\text{pose}}(a,b), \quad \text{where} \quad (14)$$

$$\mathcal{L}_{\text{match}}(a,b) = - \sum_{(i,j) \in \mathcal{T}_{ab}} \log \mathbf{P}_{ab,i,j} - \sum_{i \in \mathcal{U}_{ab}} \log \mathbf{P}_{ab,i,K_b+1} - \sum_{j \in \mathcal{V}_{ab}} \log \mathbf{P}_{ab,K_a+1,j},$$

$$\mathcal{L}_{\text{pose}}(a,b) = \|\hat{\mathbf{t}}_{a \rightarrow b} - \mathbf{t}_{a \rightarrow b}\|_2 + \lambda_{\text{rot}} \cos^{-1} \left(\frac{\text{tr}(\mathbf{R}_{a \rightarrow b}^\top \hat{\mathbf{R}}_{a \rightarrow b}) - 1}{2} \right).$$

$\mathcal{L}_{\text{match}}$ computes the negative log-likelihood of the assignment between an image pair. The labels are computed using the ground truth depth maps, camera

poses and intrinsic parameters: \mathcal{T}_{ab} is the set of matching keypoints, \mathcal{U}_{ab} and \mathcal{V}_{ab} identify unmatched keypoints from I_a and I_b , respectively. $\mathcal{L}_{\text{pose}}$ computes a transformation error between a pair of camera poses, where the translational and rotational components are balanced by λ_{rot} . $\hat{\mathbf{R}}_{a \rightarrow b}$ and $\hat{\mathbf{t}}_{a \rightarrow b}$ are a rotation matrix and translation vector computed from the pose optimization result (Sec. 3.2). Rodrigues’ formula is used to convert from axis-angle representation to rotation matrix. $\mathbf{R}_{a \rightarrow b}$ and $\mathbf{t}_{a \rightarrow b}$ define the ground truth transformation. We use the Adam optimizer [22]. Further details on the network architecture and training setup are provided in the supplementary material.

4 Results

We compare our method to baselines by evaluating indoor and outdoor pose estimation (Sec. 4.2) and matching accuracy (Sec. 4.3). Sec. 4.4 shows the effectiveness of the added components in an ablation study. Runtime considerations are part of the supplementary material.

4.1 Datasets

ScanNet [12]. Following the data generation in previous works [36,38], we sample images from the video sequence, such that the overlap to the previous image lies in $[0.4, 0.8]$. Instead of sampling a pair, we append three more images according to this overlap criterion. The resulting 5-tuples enable multi-view evaluation and provide a more realistic pose estimation scenario. The overlap is computed from ground truth poses, depth maps and intrinsic parameters.

Matterport3D [9]. Compared to ScanNet, Matterport3D view captures are much more sparse, i.e., neighboring images are 60° horizontally and 30° vertically apart. Hence, Matterport3D is a challenging dataset for the matching task. To obtain a sufficient dataset size, we relax the overlap criterion to $[0.25, 0.8]$. This challenging dataset, serves to measure robustness on the pose estimation task.

MegaDepth [24]. As in prior work [36,15], the overlap between images is the portion of co-visible 3D points of the sparse reconstruction, thus the overlap definition is different from the indoor datasets and not comparable. Overlap ranges $[0.1, 0.7]$ and $[0.1, 0.4]$ are used at train and test time, respectively [36].

4.2 Pose Estimation

Prior work, in particular SuperGlue [36], has extensively demonstrated the superiority of the GNN approach over conventional matching. Hence, we focus on comparisons to recent feature matching networks: SuperGlue [36], LoFTR [38] and COTR [21]. We additionally compare to a non-learning-based matcher, i.e., mutual nearest neighbor search on the SuperPoint [14] descriptors. This serves

Table 2. Baseline comparison and ablation study on wide-baseline indoor pose estimation on ScanNet; “cross-dataset” indicates that COTR was trained on MegaDepth.

	Rotation error AUC [%] \uparrow			Translation error AUC [%] \uparrow		
	@5°	@10°	@20°	@5cm	@10cm	@20cm
Mutual nearest neighbor	14.5	25.9	40.7	3.7	8.9	17.9
SuperGlue [36]	63.4	78.9	88.2	28.9	49.0	67.8
LoFTR [38]	72.2	83.9	90.4	40.2	59.7	75.4
COTR [21] cross-dataset	46.2	60.5	72.0	20.9	36.1	51.8
Ours w/o multi-view	68.7	81.9	89.6	35.8	56.7	73.6
Ours w/o end-to-end	66.0	80.6	89.2	31.0	51.8	70.3
Ours	72.5	84.6	91.5	41.5	61.8	77.5

Table 3. Baseline comparison and ablation study on wide-baseline indoor pose estimation on Matterport3D.

	Rotation error AUC [%] \uparrow			Translation error AUC [%] \uparrow		
	@5°	@10°	@20°	@5cm	@10cm	@20cm
Mutual nearest neighbor	0.6	2.0	5.4	0.0	0.1	0.3
SuperGlue [36]	18.5	29.6	41.7	3.4	8.5	16.9
Ours w/o multi-view	27.2	38.0	49.1	6.5	14.2	24.6
Ours w/o end-to-end	30.5	42.3	53.5	7.1	16.3	28.2
Ours	42.4	55.4	66.2	12.2	24.9	39.8

Table 4. Baseline comparison and ablation study on wide-baseline outdoor pose estimation on MegaDepth. For comparison to LoFTR, we retrain and test our model on the LoFTR data split (bottom section of the table).

	Rotation error AUC [%] \uparrow			Translation error AUC [%] \uparrow			
	@5°	@10°	@20°	@5°	@10°	@20°	
Split A	Mutual nearest neighbor	14.3	27.8	44.2	6.6	14.6	26.5
	SuperGlue [36]	70.3	77.8	83.7	53.3	64.1	73.6
	COTR [21]	61.4	69.7	77.5	45.7	56.7	66.9
	Ours w/o multi-view	74.4	80.8	86.1	58.5	68.8	77.4
	Ours w/o end-to-end	74.5	81.6	87.0	57.8	68.9	77.8
	Ours	81.1	86.8	91.2	67.7	76.6	83.6
Split B	LoFTR [38]	75.2	83.0	88.6	60.5	71.3	79.7
	Ours	89.6	93.6	95.9	74.1	82.3	88.3

to confirm the effectiveness of SuperGlue and our method, which both use SuperPoint descriptors.

For each method, the matches and confidences are used to optimize for the camera poses according to Sec. 3.2. As the baselines are designed for matching image pairs, we run them repeatedly on all 10 possible pairs of the 5-tuples and use all resulting matches in the pose optimization. The pose accuracy is evaluated



Input 5-tuples

SuperGlue [36]

LoFTR [38]

COTR [21]

Ours

Fig. 3. Reconstructions (right) from estimated camera poses on ScanNet 5-tuples (left). With multi-view matching and end-to-end training, our method successfully handles challenging pose estimation scenarios, while baselines show severe camera pose errors.

based on the area under the curve (AUC) in % at the thresholds $[5^\circ, 10^\circ, 20^\circ]$ for rotation error and $[5\text{cm}, 10\text{cm}, 20\text{cm}]$ for translation error on ScanNet and Matterport3D. As MegaDepth reconstructions are up to an unknown scale factor, the translation error is measured by the angle between translation vectors using thresholds $[5^\circ, 10^\circ, 20^\circ]$ for the AUC. For qualitative comparison we use the computed poses to fuse the 5 depth maps in a truncated signed distance field (TSDF), which is then converted into a mesh using marching cubes [25].

Quantitative results on ScanNet are shown in Tab. 2, demonstrating that our method achieves higher accuracy than baselines. The misalignments in the reconstructions (Fig. 3) reveal that the baselines struggle in presence of repetitive patterns such as the washing machines (sample 1), the pictures on the

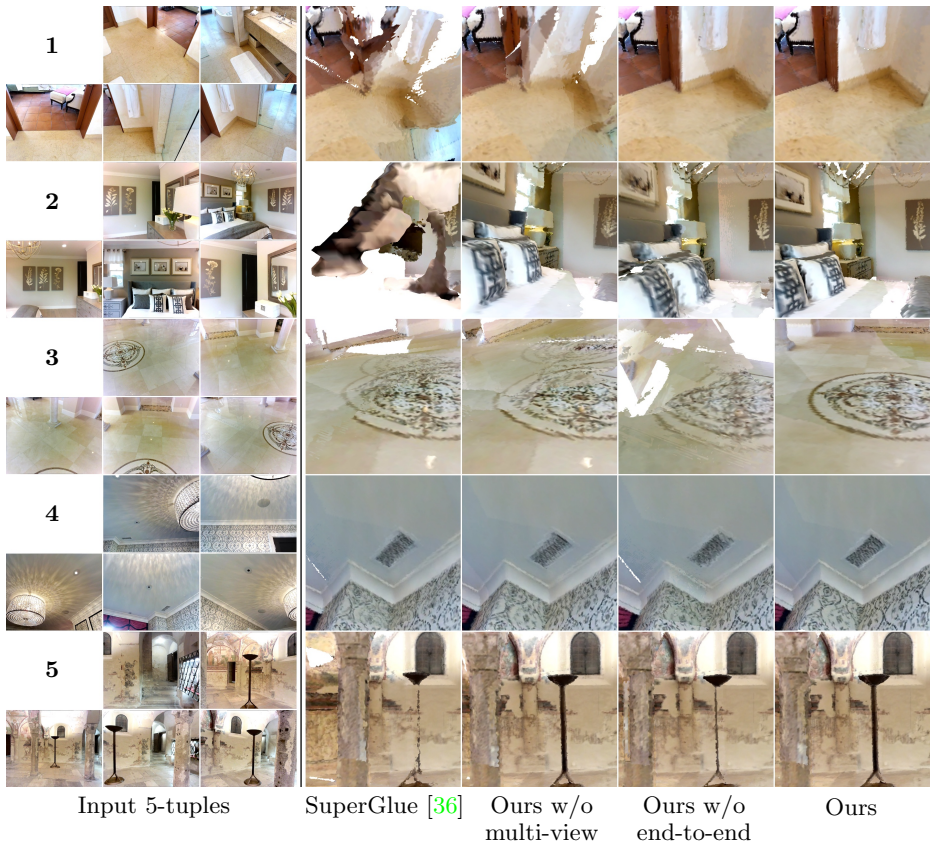


Fig. 4. Reconstructions (right) from estimated camera poses on Matterport3D 5-tuples (left). Our complete method improves camera alignment over the ablated versions and SuperGlue, showing the importance of multi-view matching and end-to-end training.

wall (sample 5) or the patterned couches (sample 6). With multi-view reasoning during matching and learned outlier rejection through end-to-end training, our approach is more robust in these situations.

Tab. 3 evaluates pose estimation on Matterport3D. The pose accuracy on Matterport3D is overall lower than on ScanNet, due to the smaller overlap between images and possibly amplified by the smaller training dataset. In this scenario, our method outperforms SuperGlue with a larger gap than on ScanNet, which shows that our approach copes better with the more challenging setting in Matterport3D. We show additional analysis in the ablation study.

Quantitative results on MegaDepth demonstrate the gain from multi-view matching and end-to-end training in the outdoor setting, leading to higher accuracy than baselines (Tab. 4). Qualitative results are provided in the supplement.

Implementation Details. COTR does not predict confidences, hence we use equal weights for all matches. For SuperGlue and LoFTR, the predicted confidences are used in the pose optimization, which we empirically found to

Table 5. Baseline comparison on wide-baseline matching accuracy on ScanNet.

	Number of matches	Epipolar error [m] ↓
Mutual nearest neighbor	192	0.373
SuperGlue [36]	207	0.158
SuperGlue [36] w/ threshold 0.2	189	0.032
LoFTR [38]	1304	0.034
COTR [21]	96	0.069
Ours	186	0.020

perform better than thresholding. Further implementation detail is available in the supplemental.

4.3 Matching

To avoid manual setting of confidence thresholds, the matching accuracy is evaluated by computing the weighted mean of the epipolar error e on image pairs:

$$e = \frac{\sum_{m=1}^M w_m e_m}{\sum_{m=1}^M w_m}, \quad (15)$$

where M is the number of matches between an image pair, e_m the symmetric epipolar error of a match and w_m its confidence. The epipolar error and the average number of detected matches on ScanNet are listed in Tab. 5. As SuperGlue explicitly proposes a confidence threshold at 0.2 to determine valid matches, we also report this version of the baseline. While our method achieves the lowest epipolar error, LoFTR produces a much higher number of matches. This shows that the number of matches is not a reliable indicator for pose accuracy, but rather accurate matches and confidences are beneficial.

4.4 Ablation Study

The quantitative results on ScanNet, Matterport3D and MegaDepth (Tabs. 2 to 4), show that the full version of our method achieves the best performance. This is consistent with the qualitative results in Fig. 4.

Without Multi-View. Omitting multi-view in the GNN causes an average performance drop of 3.9% on ScanNet and 13.6% on Matterport3D. This suggests that the importance of multi-view increases with decreasing overlap between images. Intuitively, the multi-view receptive field supports information flow from other views to bridge gaps, where the overlap is small. Fig. 4 shows the notably improved camera alignment through multi-view input.

Without End-to-End. Omitting end-to-end training drops the average performance by 6.8% on ScanNet and 10.5% on Matterport3D. This shows that end-to-end training enables the learning of reliable outlier down-weighting, which is even more beneficial in the difficult Matterport3D scenarios. Lack of end-to-end training is visible in the reconstructions (Fig. 4), e.g., the misaligned pattern on the floor (sample 3) or the failure to reconstruct thin objects (sample 5).

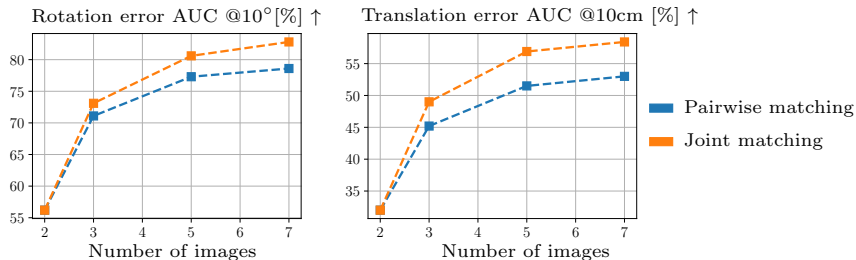


Fig. 5. Pose error AUC on sequences of 9 images on ScanNet using variable number of images in pairwise or joint matching.

Variable Number of Input Views. In Fig. 5, we investigate the impact of the number of images used for matching, both in pairwise (ours w/o multi-view) and joint (our full version) fashion. The experiment is conducted on sequences of 9 images which are generated on ScanNet as described in Sec. 4.1. The results show that pose accuracy improves, when matching across a larger span of neighboring images. The curves, however, plateau when a larger window size does not bring any more relevant images into the matching. Additionally, the results show the benefit of joint matching in a single graph as opposed to matching all possible image pairs individually.

4.5 Limitations

Our method builds on SuperGlue [36] and improves pose estimation accuracy and robustness to small image overlap. Here, one of our contributions is the end-to-end differentiability of the pose optimization that guides the matching network. While this significantly improves matching quality, we currently only backpropagate gradients to the matching network but do not update keypoint descriptors; i.e., we use existing SuperPoint [14]. However, we believe that jointly training feature descriptors is a promising avenue to even further improve performance.

5 Conclusion

We have presented a method that couples multi-view feature matching and pose optimization into an end-to-end trainable pipeline. Using a graph neural network, we match features across multiple views in a joint fashion, which increases global awareness of the matching process. Combined with differentiable pose optimization, gradients inform the matching network, which learns to produce valuable, outlier-free matches for pose estimation. The experiments show that our method improves both pose and matching accuracy compared to prior work. In particular, we observe increased robustness in challenging settings, such as in presence of repetitive structure or small image overlap. Overall, we believe that our end-to-end approach is an important stepping stone towards an end-to-end trained SLAM method.

Acknowledgements

This project is funded by a TUM-IAS Rudolf Mößbauer Fellowship, the ERC Starting Grant Scan2CAD (804724), and the German Research Foundation (DFG) Grant Making Machine Learning on Static and Dynamic 3D Data Practical. We thank Angela Dai for the video voice-over.

References

1. Agarwal, S., Furukawa, Y., Snavely, N., Simon, I., Curless, B., Seitz, S.M., Szeliski, R.: Building rome in a day. *Communications of the ACM* **54**(10), 105–112 (2011) [3](#)
2. Baráth, D., Matas, J.: Magsac: Marginalizing sample consensus. 2019 IEEE/CVF Conference on Computer Vision and Pattern Recognition (CVPR) pp. 10189–10197 (2019) [3](#)
3. Bhowmik, A., Gumhold, S., Rother, C., Brachmann, E.: Reinforced feature points: Optimizing feature detection and description for a high-level task. 2020 IEEE/CVF Conference on Computer Vision and Pattern Recognition (CVPR) pp. 4947–4956 (2020) [3](#)
4. Bian, J., Lin, W.Y., Matsushita, Y., Yeung, S.K., Nguyen, T.D., Cheng, M.M.: Gms: Grid-based motion statistics for fast, ultra-robust feature correspondence. 2017 IEEE Conference on Computer Vision and Pattern Recognition (CVPR) pp. 2828–2837 (2017) [3](#)
5. Blanco, J.L.: A tutorial on se(3) transformation parameterizations and on-manifold optimization. University of Malaga, Tech. Rep (09 2010) [8](#)
6. Brachmann, E., Rother, C.: Neural-guided ransac: Learning where to sample model hypotheses. 2019 IEEE/CVF International Conference on Computer Vision (ICCV) pp. 4321–4330 (2019) [3](#)
7. Cavalli, L., Larsson, V., Oswald, M.R., Sattler, T., Pollefeys, M.: Handcrafted outlier detection revisited. In: ECCV (2020) [3](#)
8. Cech, J., Matas, J., Perdoch, M.: Efficient sequential correspondence selection by cosegmentation. *IEEE Transactions on Pattern Analysis and Machine Intelligence* **32**, 1568–1581 (2008) [3](#)
9. Chang, A.X., Dai, A., Funkhouser, T.A., Halber, M., Nießner, M., Savva, M., Song, S., Zeng, A., Zhang, Y.: Matterport3d: Learning from rgb-d data in indoor environments. 3DV (2017) [2](#), [9](#), [20](#), [21](#)
10. Choi, S., Zhou, Q.Y., Koltun, V.: Robust reconstruction of indoor scenes. In: IEEE Conference on Computer Vision and Pattern Recognition (CVPR) (2015) [4](#)
11. Cuturi, M.: Sinkhorn distances: Lightspeed computation of optimal transport. In: NIPS (2013) [7](#)
12. Dai, A., Chang, A.X., Savva, M., Halber, M., Funkhouser, T.A., Nießner, M.: Scannet: Richly-annotated 3d reconstructions of indoor scenes. CVPR (2017) [2](#), [9](#), [20](#)
13. Dai, A., Nießner, M., Zollhöfer, M., Izadi, S., Theobalt, C.: Bundlefusion: Real-time globally consistent 3d reconstruction using on-the-fly surface reintegration. *ACM Transactions on Graphics (ToG)* **36**(4), 1 (2017) [3](#)
14. DeTone, D., Malisiewicz, T., Rabinovich, A.: Superpoint: Self-supervised interest point detection and description. 2018 IEEE/CVF Conference on Computer Vision and Pattern Recognition Workshops (CVPRW) pp. 337–33712 (2018) [3](#), [4](#), [9](#), [14](#), [20](#)
15. Dusmanu, M., Rocco, I., Pajdla, T., Pollefeys, M., Sivic, J., Torii, A., Sattler, T.: D2-net: A trainable cnn for joint description and detection of local features. 2019 IEEE/CVF Conference on Computer Vision and Pattern Recognition (CVPR) pp. 8084–8093 (2019) [3](#), [9](#)
16. Duvenaud, D., Maclaurin, D., Aguilera-Iparraguirre, J., Gómez-Bombarelli, R., Hirzel, T., Aspuru-Guzik, A., Adams, R.: Convolutional networks on graphs for learning molecular fingerprints. *Advances in Neural Information Processing Systems (NIPS)* (2015) [6](#)

17. Fischler, M.A., Bolles, R.C.: Random sample consensus: a paradigm for model fitting with applications to image analysis and automated cartography. *Commun. ACM* **24**, 381–395 (1981) [3](#)
18. Gehring, J., Auli, M., Grangier, D., Yarats, D., Dauphin, Y.: Convolutional sequence to sequence learning. In: *ICML (2017)* [5](#)
19. Gilmer, J., Schoenholz, S.S., Riley, P.F., Vinyals, O., Dahl, G.E.: Neural message passing for quantum chemistry. In: *ICML (2017)* [6](#)
20. Han, L., Ji, M., Fang, L., Nießner, M.: Regnet: Learning the optimization of direct image-to-image pose registration. *arXiv preprint arXiv:1812.10212* (2018) [4](#)
21. Jiang, W., Trulls, E., Hosang, J., Tagliasacchi, A., Yi, K.M.: COTR: Correspondence Transformer for Matching Across Images. In: *ICCV (2021)* [2](#), [3](#), [9](#), [10](#), [11](#), [13](#), [19](#), [21](#)
22. Kingma, D.P., Ba, J.: Adam: A method for stochastic optimization. *CoRR* (2015) [9](#)
23. Li, X., Han, K., Li, S., Prisacariu, V.A.: Dual-resolution correspondence networks. *NeurIPS* (2020) [3](#)
24. Li, Z., Snavely, N.: Megadepth: Learning single-view depth prediction from internet photos. 2018 *IEEE/CVF Conference on Computer Vision and Pattern Recognition* pp. 2041–2050 (2018) [2](#), [9](#), [20](#)
25. Lorensen, W.E., Cline, H.E.: Marching cubes: A high resolution 3d surface construction algorithm. *Proceedings of the 14th annual conference on Computer graphics and interactive techniques* (1987) [11](#)
26. Lowe, D.: Distinctive image features from scale-invariant keypoints. *International Journal of Computer Vision* (2004) [3](#), [4](#)
27. Ma, J., Zhao, J., Jiang, J., Zhou, H., Guo, X.: Locality preserving matching. *International Journal of Computer Vision* pp. 512–531 (2018) [3](#)
28. Ono, Y., Trulls, E., Fua, P.V., Yi, K.M.: Lf-net: Learning local features from images. In: *NeurIPS* (2018) [3](#)
29. Pais, G.D., Ramalingam, S., Govindu, V.M., Nascimento, J.C., Chellappa, R., Miraldo, P.: 3dregnet: A deep neural network for 3d point registration. In: *Proceedings of the IEEE/CVF conference on computer vision and pattern recognition*. pp. 7193–7203 (2020) [4](#)
30. Raguram, R., Frahm, J.M., Pollefeys, M.: A comparative analysis of ransac techniques leading to adaptive real-time random sample consensus. In: *ECCV* (2008) [3](#)
31. Ranftl, R., Koltun, V.: Deep fundamental matrix estimation. In: *ECCV* (2018) [3](#)
32. Revaud, J., Weinzaepfel, P., de Souza, C.R., Pion, N., Csurka, G., Cabon, Y., Humenberger, M.: R2d2: Repeatable and reliable detector and descriptor. *Advances in Neural Information Processing Systems* (2019) [3](#)
33. Rocco, I., Arandjelović, R., Sivic, J.: Efficient neighbourhood consensus networks via submanifold sparse convolutions. In: *ECCV* (2020) [3](#)
34. Rocco, I., Cimpoi, M., Arandjelović, R., Torii, A., Pajdla, T., Sivic, J.: Neighbourhood consensus networks. In: *NeurIPS* (2018) [3](#)
35. Rublee, E., Rabaud, V., Konolige, K., Bradski, G.R.: Orb: An efficient alternative to sift or surf. 2011 *International Conference on Computer Vision* pp. 2564–2571 (2011) [3](#)
36. Sarlin, P.E., DeTone, D., Malisiewicz, T., Rabinovich, A.: Superglue: Learning feature matching with graph neural networks. 2020 *IEEE/CVF Conference on Computer Vision and Pattern Recognition (CVPR)* pp. 4937–4946 (2020) [2](#), [3](#), [4](#), [5](#), [6](#), [7](#), [8](#), [9](#), [10](#), [11](#), [12](#), [13](#), [14](#), [19](#), [20](#), [21](#)

37. Sinkhorn, R., Knopp, P.: Concerning nonnegative matrices and doubly stochastic matrices. *Pacific Journal of Mathematics* pp. 343–348 (1967) [7](#)
38. Sun, J., Shen, Z., Wang, Y., Bao, H., Zhou, X.: Loftr: Detector-free local feature matching with transformers. 2021 IEEE/CVF Conference on Computer Vision and Pattern Recognition (CVPR) pp. 8918–8927 (2021) [2](#), [3](#), [9](#), [10](#), [11](#), [13](#), [21](#)
39. Tang, C., Tan, P.: Ba-net: Dense bundle adjustment network. arXiv preprint arXiv:1806.04807 (2018) [4](#)
40. Triggs, B., McLauchlan, P.F., Hartley, R.I., Fitzgibbon, A.W.: Bundle adjustment—a modern synthesis. In: *International workshop on vision algorithms*. pp. 298–372. Springer (1999) [3](#)
41. Tuytelaars, T., Gool, L.V.: Wide baseline stereo matching based on local, affinely invariant regions. In: *BMVC* (2000) [3](#)
42. Tyszkiewicz, M.J., Fua, P., Trulls, E.: Disk: Learning local features with policy gradient. *Advances in Neural Information Processing Systems* (2020) [3](#)
43. Ummenhofer, B., Zhou, H., Uhrig, J., Mayer, N., Ilg, E., Dosovitskiy, A., Brox, T.: Demon: Depth and motion network for learning monocular stereo. In: *Proceedings of the IEEE conference on computer vision and pattern recognition*. pp. 5038–5047 (2017) [4](#)
44. Vaswani, A., Shazeer, N., Parmar, N., Uszkoreit, J., Jones, L., Gomez, A.N., Kaiser, L.u., Polosukhin, I.: Attention is all you need. In: *Advances in Neural Information Processing Systems* (2017) [3](#), [5](#), [6](#)
45. Yi, K.M., Trulls, E., Lepetit, V., Fua, P.V.: Lift: Learned invariant feature transform. *ECCV* (2016) [3](#)
46. Yi, K.M., Trulls, E., Ono, Y., Lepetit, V., Salzmann, M., Fua, P.V.: Learning to find good correspondences. 2018 IEEE/CVF Conference on Computer Vision and Pattern Recognition pp. 2666–2674 (2018) [3](#)
47. Zach, C.: Robust bundle adjustment revisited. In: *European Conference on Computer Vision*. pp. 772–787. Springer (2014) [4](#)
48. Zhang, J., Sun, D., Luo, Z., Yao, A., Zhou, L., Shen, T., Chen, Y., Quan, L., Liao, H.: Learning two-view correspondences and geometry using order-aware network. 2019 IEEE/CVF International Conference on Computer Vision (ICCV) pp. 5844–5853 (2019) [3](#)

A Qualitative Results on MegaDepth

Fig. 6 shows qualitative results from the ablation study and baseline comparison on MegaDepth dataset. The full version of our method accurately estimates camera poses even across large viewpoint changes (e.g., sample 4), and strong appearance variations (e.g., samples 1 and 2).

B Runtime

Our method takes on average 207ms for matching a 5-tuple, which corresponds to matching 10 image pairs. SuperGlue requires on average 40ms for matching one pair, which shows that inference time correlates well with the number of GNN messages (Tab. 1). LoFTR takes on average 89ms for a pair and COTR is much slower with 35s. Although we did not optimize our implementation for speed, the measurement shows that it is suited for real-time application. We believe that the coupling of multi-view matching with pose optimization fits particularly well for keyframe alignment in reconstruction or SLAM. An alternative pose optimization module using relative poses, e.g., from inertial sensors, instead of depth measurements can also be realized. All runtime is measured on a Nvidia GeForce RTX 2080.

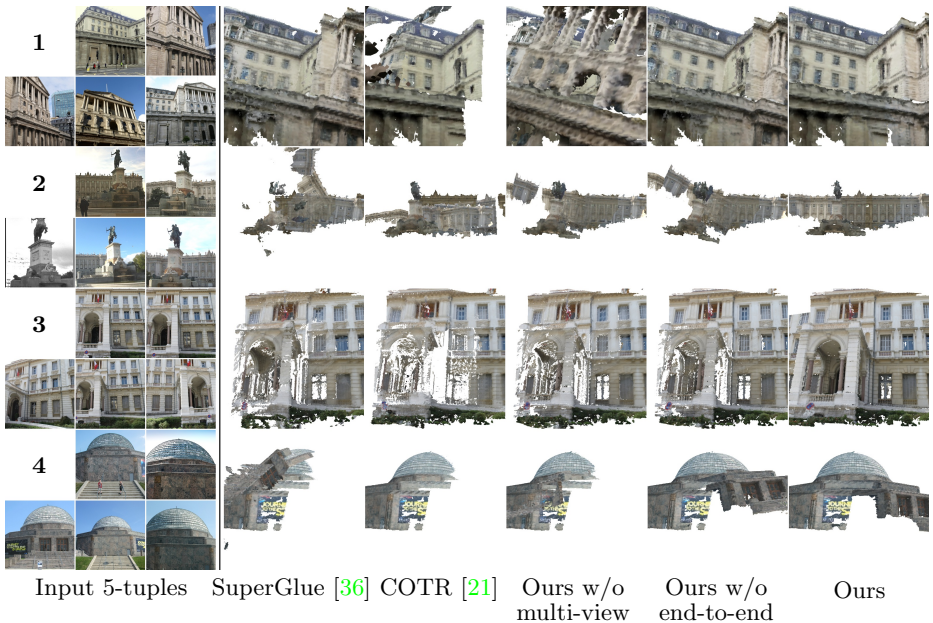


Fig. 6. Reconstructions (right) from estimated camera poses on MegaDepth 5-tuples (left). With multi-view matching and end-to-end training, our method successfully estimates camera poses in challenging outdoor scenarios, while baselines show misalignment.

C Architecture Details

Our multi-view matching network builds up on the SuperGlue [36] architecture and uses the following parameters:

Keypoint Encoder. The input visual descriptors from SuperPoint [14] have size $D = 256$. The graph nodes equally have an embedding size of D . Hence, the keypoint encoder F_{encode} maps a keypoint’s image coordinates and confidence score to D dimensions. It is a MLP, composed of five layers with 32, 64, 128, 256 and D channels. Each layer, except the last, uses batch normalization and ReLU activation.

Graph Attention Network. The GNN has $L = 9$ layers. The layers alternate between message exchange along self-edges and message exchange along cross-edges, such that the first and last layers perform updates along self-edges. The attentional aggregation of incoming messages from other nodes uses multi-head attention with four heads. The resulting messages have size D , like the node embeddings. The MLP F_{update} , which computes the update to the receiving node, operates on the concatenation of the current node embedding with the incoming message. It has two layers with $2D$ and D channels. Batch normalization and ReLU activation are employed between the two layers.

Partial Assignment. We use 100 iterations of the Sinkhorn algorithm to determine the partial assignment matrices.

Pose Optimization. The camera poses are optimized by conducting $T = 10$ Gauss-Newton updates.

D Training Details

Two-Stage Training. Our end-to-end pipeline is trained in two stages. The first stage uses the loss term on the matching result $\mathcal{L}_{\text{match}}$. The second stage additionally employs the pose loss $\mathcal{L}_{\text{pose}}$. Stage 1 is trained until the validation match loss converges, stage 2 until the validation pose loss converges. On ScanNet [12]/ Matterport3D [9]/ MegaDepth [24] the training takes 25/ 228/ 71 epochs for stage 1 and 4/ 7/ 11 epochs for stage 2. We found that the training on MegaDepth benefits from initializing the network parameters to the network parameters after the first ScanNet training stage. During stage 2 we linearly increase the weight of $\mathcal{L}_{\text{pose}}$ from 0 to 2000 on the indoor datasets, and from 0 to 685 on MegaDepth, while linearly decreasing the weight of $\mathcal{L}_{\text{match}}$ from 1 to 0, over a course of 40000 iterations. The balancing factor of the rotation term in $\mathcal{L}_{\text{pose}}$ is set to $\lambda_{\text{rot}} = 2$ on the indoor datasets and $\lambda_{\text{rot}} = 6.75$ on MegaDepth. We use the Adam optimizer with learning rate 0.0001. The learning rate is exponentially decayed with a factor of 0.999992 starting after 100k iterations.

Ground Truth Generation. The ground truth matches \mathcal{T}_{ab} and sets of unmatched keypoints \mathcal{U}_{ab} , \mathcal{V}_{ab} of an image pair are computed by projecting the detected keypoints from each image to the other, resulting in a reprojection error matrix. Keypoint pairs where the reprojection error is both minimal and

smaller than 5 pixels in both directions are considered matches. Unmatched key-points must have a minimum reprojection error greater than 15 pixels on the indoor datasets and greater than 10 pixels on MegaDepth.

Input Data. We train on 5-tuples with a batch size of 24 on indoor data and with a batch size of 4 on outdoor data. The image size is 480×640 on ScanNet, 512×640 on Matterport3D and 640×640 on MegaDepth. The SuperPoint network is configured to detect keypoints with a non-maximum suppression radius of 4/ 3 on indoor/ outdoor data. On the indoor datasets we use 400 keypoints per image during training time: first, keypoints above a confidence threshold of 0.001 are sampled, second, if there are fewer than 400, the remainder is filled with random image points and confidence 0 as a data augmentation. On MegaDepth the same procedure is applied to sample 1024 keypoints using confidence threshold 0.005. At test time on indoor/ outdoor data, we use up to 1024/ 2048 keypoints above the mentioned confidence thresholds.

Dataset Split. On ScanNet and Matterport3D we use the official dataset split. On MegaDepth we use scenes 0016, 0047, 0058, 0064, 0121, 0129, 0133, 0168, 0175, 0178, 0181, 0185, 0186, 0204, 0205, 0212, 0217, 0223, 0229 for validation, 0271, 0285, 0286, 0294, 0303, 0349, 0387, 0412, 0443, 0482, 0768, 1001, 3346, 5014, 5015, 5016, 5018 for testing and the remaining scenes for training. This way on ScanNet/ Matterport3D/ MegaDepth we obtain 240k/ 20k/ 15k 5-tuples for training, 62k/ 2200/ 1200 for validation and 1500/ 1500/ 1000 for testing.

E Baseline Comparison

In the baseline comparison we use the network weights trained by the authors of SuperGlue [36], LoFTR [38] and COTR [21]. There are SuperGlue and LoFTR models trained on ScanNet and on MegaDepth, as well as a COTR model trained on MegaDepth. We additionally train a SuperGlue model on Matterport3D [9].